

1 **Joint inversion of satellite-detected tidal and magnetospheric**
2 **signals constrains electrical conductivity and water content of**
3 **the upper mantle and transition zone**

4 **A. V. Grayver¹, F. D. Munch¹, A. V. Kuvshinov¹, A. Khan¹, T. J. Sabaka², L.**
5 **Tøffner-Clausen³**

6 ¹Institute of Geophysics, ETH Zürich, Switzerland.

7 ²Geodesy and Geophysics Laboratory, NASA/GSFC, USA

8 ³DTU Space, Technical University of Denmark, Denmark

9 **Key Points:**

10

11

12

13

14

15

- Joint inversion of Swarm and CHAMP data from magnetospheric and ocean tidal currents reveals global features of the upper mantle and MTZ.
- Integrated imaging of the mantle electrical conductivity from multiple sources significantly improves resolution.
- Retrieved conductivity profiles are compatible with a pyrolytic composition and a moderate mantle water content.

Abstract

We present a new global electrical conductivity model of Earth's mantle. The model was derived by using a novel methodology, which is based on inverting satellite magnetic field measurements from different sources simultaneously. Specifically, we estimated responses of magnetospheric origin and ocean tidal magnetic signals from the most recent Swarm and CHAMP data. The challenging task of properly accounting for the ocean effect in the data was addressed through full three-dimensional solution of Maxwell's equations. We show that simultaneous inversion of magnetospheric and tidal magnetic signals results in a model with much improved resolution. Comparison with laboratory-based conductivity profiles shows that obtained models are compatible with a pyrolytic composition and a water content of 0.01 wt% and 0.1 wt% in the upper mantle and transition zone, respectively.

1 Introduction

Electromagnetic (EM) sounding is an important technique for studying Earth's interior and its material properties. It can be used to infer electrical conductivity in depth and map its lateral variations within the Earth, thereby carrying information about composition, temperature and presence of water or melt in the mantle [Karato, 2011; Katsura and Yoshino, 2015; Khan, 2016]. The unique characteristic of EM methods is the wide frequency range, corresponding to sounding depths from crust to lower mantle. However, across this wide frequency range several excitation mechanisms co-exist [Kuvshinov, 2008]. This requires adjustments in the source parametrization during data processing and modeling stages. Therefore, interpretation of these data is usually done separately, resulting in reduced resolution of individual models and potentially causing inconsistencies between them.

Simultaneous inversion of multiple data sets from different sources should lead to improved resolution and smaller uncertainties, and, as a consequence, additional constraints on the fundamental aspects of the composition, structure, and dynamics of the Earth. For instance, Egbert *et al.* [1992] and Bahr *et al.* [1993] estimated responses using ionospheric and magnetospheric signals, and obtained regional conductivity models of the upper and lower mantle with better resolutions due to wider frequency range of the combined responses. However, these studies used only land observatory data. Since then, operation of low-orbit satellites (Oersted, CHAMP, SAC-C, Swarm) [Olsen *et al.*, 2013] has provided a wealth of data opening new opportunities for mantle conductivity studies. In contrast to land observatories, processing of data coming from constantly moving satellites is more challenging, since it requires a careful separation of the magnetic fields from different sources. Recently, new data processing approaches have experienced a significant progress [Sabaka *et al.*, 2015], enabling the usage of both time-varying magnetospheric and tidal magnetic fields for global EM sounding. However, sensitivity of the methods depends on frequency content and mechanism of excitation. For instance, long period (periods > 1.5 days) magnetospheric responses are more sensitive to the conductivity in the mantle transition zone (MTZ) and below [Kuvshinov and Olsen, 2006; Velímský *et al.*, 2006; Civet *et al.*, 2015], whereas tidal magnetic signals, specifically signals due to lunar principal semi-diurnal M_2 tide, are more sensitive to upper mantle conductivity [Grayver *et al.*, 2016]. As a consequence, simultaneous inversion is expected to provide improved depth resolution. To corroborate this here, we perform inversions of magnetic data derived from the most recent satellite data and compare individual and joint inversion results, in addition to comparison with laboratory-based conductivity profiles for the purpose of making thermo-chemical inferences.

62 **2 Methods**63 **2.1 Satellite data**64 **2.1.1 Magnetospheric responses**

65 For periods longer than one day, signals due to magnetospheric ring current dominates
 66 the measured time-varying magnetic fields [cf. *Püthe et al.*, 2015a]. These signals are con-
 67 conventionally described by the first zonal spherical harmonic. In this work, we derived magne-
 68 tospheric responses through the so called $Q_1^0(\omega)$ -response [e.g. *Püthe and Kuvshinov*, 2013],
 69 which relates frequency-dependent inducing, $\epsilon_1^0(\omega)$, and induced, $i_1^0(\omega)$, coefficients as

$$i_1^0(\omega) = Q_1^0(\omega)\epsilon_1^0(\omega). \quad (1)$$

70 From this, the global C_1 -response [e.g. *Olsen*, 1999] on the surface of the Earth can be
 71 calculated as

$$C_1(\omega) = \frac{a}{2} \frac{1 - 2Q_1^0(\omega)}{1 + Q_1^0(\omega)}. \quad (2)$$

72 Note that for a radially homogeneous Earth, C_1 -responses exhibit monotonic growth
 73 with respect to period ($T = \frac{2\pi}{\omega}$).

74 To quantify the degree of correlation between the inducing and induced coefficients,
 75 we used squared coherence given by

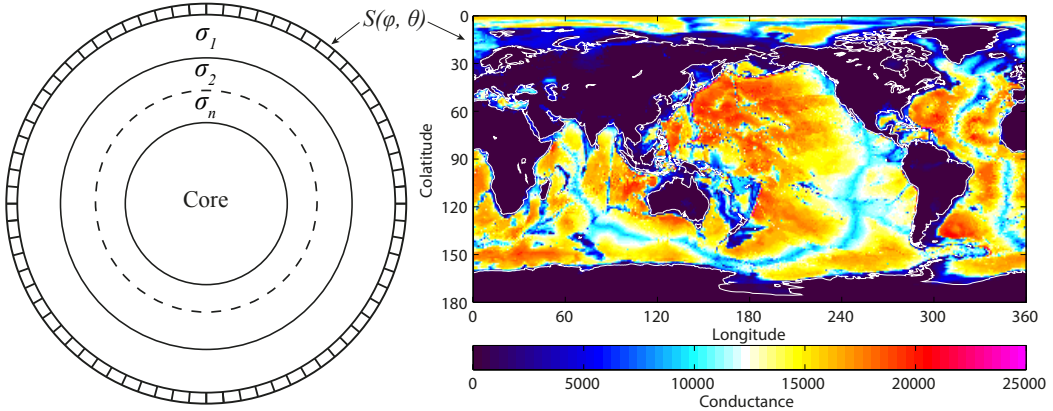
$$\text{coh}^2(\omega) = \frac{|\langle i_1^0(\omega), \epsilon_1^0(\omega) \rangle|^2}{\langle i_1^0(\omega), i_1^0(\omega) \rangle \langle \epsilon_1^0(\omega), \epsilon_1^0(\omega) \rangle}, \quad (3)$$

76 where $\langle \cdot, \cdot \rangle$ stands for inner product between two vectors. In this context, vectors are given by
 77 a set of the Fourier-transformed windows of $i_1^0(t)$ and $\epsilon_1^0(t)$ time-series. The closer this value
 78 to its upper bound of one, the more variability in $i_1^0(\omega)$ can be explained by the variability in
 79 $\epsilon_1^0(\omega)$

80 **2.1.2 Tidal magnetic signals**

81 The tidally-induced flow of the electrically conductive ocean water in Earth's main
 82 magnetic field generates electric currents, which in turn induce secondary EM field in the
 83 subsurface as a result of which the total magnetic field measured on land or at a satellite car-
 84 rries information about subsurface electrical structure. In contrast to other conventional EM
 85 sources of ionospheric and magnetospheric origin, which are inductively coupled with the
 86 Earth, the unique characteristic of the motionally-induced ocean currents is its galvanic cou-
 87 pling with the Earth. This enhances sensitivity to the resistive subsurface structures since the
 88 induced fields are influenced by the toroidal (galvanic) part of the tidal primary EM field.

89 Despite small amplitude, tidal magnetic signals due to the semi-diurnal lunar M_2 tide
 90 (period of 12 hours and 25 minutes) have been reliably extracted from satellite measure-
 91 ments using the Comprehensive Inversion approach based on the simultaneous robust least-
 92 squares estimators of different contributions (core, crust, etc.) and careful pre-selection of
 93 data [*Sabaka et al.*, 2015, 2016]. They were used to retrieve upper mantle conductivity under
 94 the oceanic crust [*Grayver et al.*, 2016]. The inverted signals are represented by the radial
 95 magnetic field component $B_r^{M_2}$ at the satellite altitude.



97 **Figure 1.** Model parametrization adopted in this study. The model consists of a laterally-varying top-most
 98 conductivity layer and a number of laterally-homogeneous conductivity layers underneath.

96 2.2 Forward modeling

99 In this work, we focus on determining the radial conductivity structure under the oceans
 100 and continents. However, to accurately calculate electromagnetic responses due to magneto-
 101 spheric or tidally-induced oceanic currents, it is essential to account for non-uniform oceans
 102 [Everett *et al.*, 2003; Kuvshinov, 2008]. To this end, we added a heterogeneous conductivity
 103 layer corresponding to oceans and continents on top of the laterally homogeneous model
 104 (Figure 1). Calculating EM field for such a 3D model requires solution of Maxwell's equa-
 105 tions

$$106 \mu_0^{-1} \nabla \times \vec{B} = \sigma \vec{E} + \vec{j}^{\text{ext}}, \\ 107 \nabla \times \vec{E} = i\omega \vec{B}, \quad (4)$$

108 where \vec{E} and \vec{B} are electric and magnetic fields, respectively; μ_0 is magnetic permeability of
 109 vacuum; σ electrical conductivity; ω the angular frequency and \vec{j}^{ext} the extraneous current.
 110 We assume $e^{-i\omega t}$ sign convention.

111 To solve system (4) numerically, we used global solver [Kuvshinov, 2008] based on the
 112 integral equation approach.

113 For tidal flow, the extraneous current is confined to the oceans and is given by

$$114 \vec{j}^{\text{ext}}(\phi, \theta) = \sigma_s(\phi, \theta) \left(\vec{v}(\phi, \theta) \times \vec{B}^{\text{main}}(\phi, \theta) \right), \quad (5)$$

115 where σ_s is the conductivity of seawater, \vec{B}^{main} is Earth's main (core) magnetic field, $\vec{v} = \vec{u}/h$, h is the height of the water column and \vec{u} is the depth-integrated seawater velocity due
 116 to tidal forces. Symbols ϕ and θ denote, respectively longitude and co-latitude. See Grayver
 117 *et al.* [2016] for more details about eq. 5 individual terms.

118 For the global $Q_1^0(\omega)$ response, which we need to derive the global C_1 -response, the
 119 extraneous source current is parameterized using a single $S_1^0(\theta) = \cos \theta$ spherical harmonic.
 120 The source is then represented as a current sheet located above the Earth's surface. Once sys-
 121 tem (4) is solved for the given current distribution, and the radial component of the magnetic
 field, B_r , at the Earth's surface is obtained, the $Q_1^0(\omega)$ is expressed via surface integral in
 geomagnetic coordinates as

$$122 Q_1^0(\omega) = \frac{3}{8\pi} \iint_S \left(B_r(\omega, \vec{r}) - \vec{B}_r^{\text{ext}}(\omega, \vec{r}) \right) S_1^0(\theta_{\text{GM}}) dS, \quad (6)$$

122 where B_r^{ext} is the external magnetic field, $\vec{r} = (r = a, \phi_{GM}, \theta_{GM})$ is the position vector in
 123 geomagnetic coordinates on the surface of the Earth, respectively, and $a = 6371.2$ km is the
 124 mean radius of the Earth.

125 2.3 Stochastic inversion of multi-source data

126 The unknown conductivity values $\sigma_1 \cdots \sigma_N$ (Figure 1) can be estimated from satellite
 127 responses by solving a non-linear inverse problem, which we formulate as a minimization
 128 task

$$\underset{\mathbf{m}}{\text{argmin}} \left(\frac{\phi_d(\mathbf{m})}{2} + \frac{\beta}{p_m} \sum_{i=1}^M |\mathbf{l}_i \mathbf{m}|^{p_m} \right), \quad (7)$$

129 where $\mathbf{m} = [\lambda(\sigma_1) \cdots \lambda(\sigma_M)] \in \mathbb{R}^M$ is the vector of unknown model parameters and $\lambda(\cdot)$
 130 represents a log-based transformation ensuring positivity of the argument [e.g. *Key*, 2016];
 131 β is a regularization parameter; \mathbf{l}_i is a regularization operator for the i -th model parameter;
 132 and scalar p_m controls the norm of the regularization term. By varying p_m , one retrieves
 133 different regularization norms, ranging from smooth L_2 -norm ($p_m = 2$) to structurally sparse
 134 L_1 -norm ($p_m = 1$) solutions. Special attention is paid to the data misfit term given by

$$\phi_d(\mathbf{m}) = \sum_{k \in \mathcal{M}} \left(\frac{1}{N_k} \sum_{i=1}^{N_k} |w_i^k (f_i^k(\mathbf{m}) - d_i^k)|^2 \right), \quad (8)$$

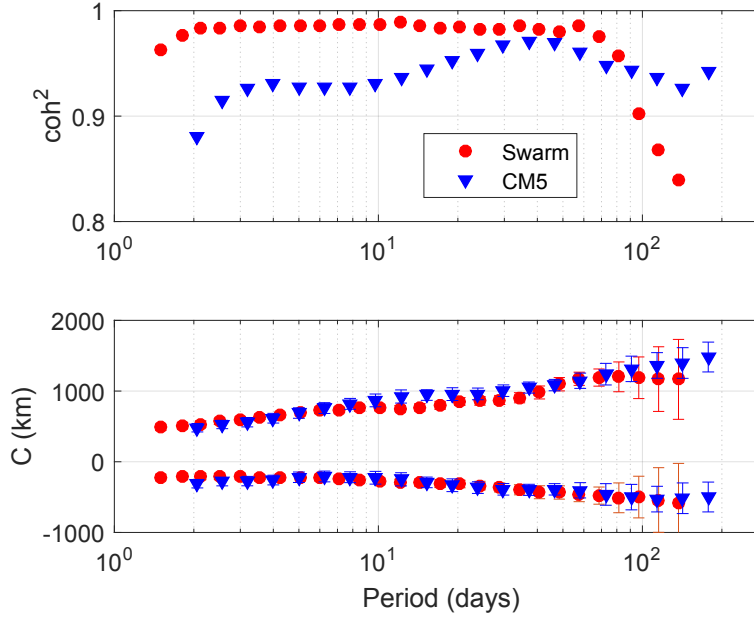
135 where \mathcal{M} is a set of methods and $\mathbf{w}^k, \mathbf{f}^k(\mathbf{m})$, and \mathbf{d}^k are corresponding data weights (recipro-
 136 cal of uncertainties), forward operator, and observed data, respectively. Note that normaliz-
 137 ing with the number of actual measurements (N_k) is an important aspect that helps balance
 138 contributions of different methods in the total misfit term of the minimized functional. In
 139 general, the approach can be extended to any number of methods, but here is limited to meth-
 140 ods discussed in Section 2.1.

141 Finally, the minimization problem (7) is solved by using a stochastic optimization algo-
 142 rithm as described in *Grayver and Kuvshinov* [2016].

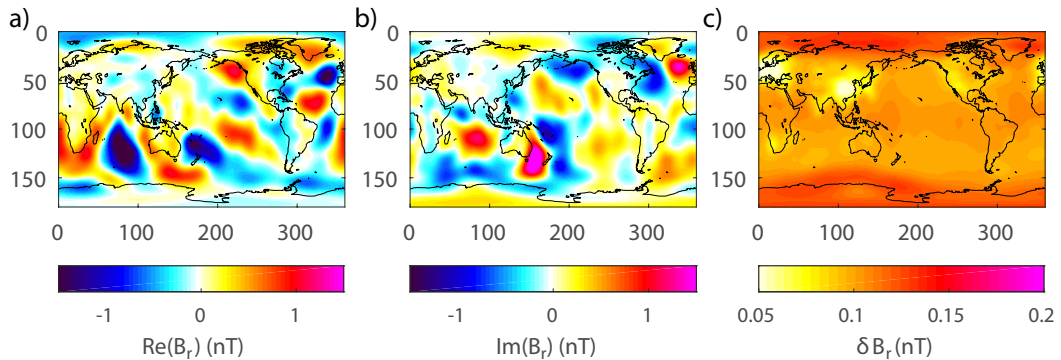
143 3 Results

144 3.1 Satellite data

145 To estimate global C_1 -responses, we used satellite magnetic measurements. The re-
 146 sponds were derived from 37 months (from Dec 2013 to Jan 2017) of Swarm data for peri-
 147 ods of 1.5 - 87 days (Figure 2). For periods > 90 days, we took responses derived from the
 148 much longer CM5 (combined CHAMP, Oersted and SAC-C data) time-series [Sabaka *et al.*,
 149 2015]. In order to better account for the complexity of the source, the magnetospheric time
 150 series were parametrized using spherical harmonics up to degree $n = 2$ and order $m = 1$, al-
 151 though only the term corresponding to the $n = 1, m = 0$ was used to estimate C_1 -responses in
 152 the frequency domain. This choice is justified since this term is dominant [e.g. *Shore* *et al.*,
 153 2016] and most sensitive to the radial structure of the Earth [Kuvshinov, 2008], which we
 154 aim to recover in this study. Figure 2 shows statistically estimated responses, their uncer-
 155 tainties and squared coherencies. Clearly, using Swarm data results in higher coherency for peri-
 156 ods up to ≈ 90 days. For longer periods, coherency drops because of still insufficient length
 157 of the Swarm time series. In contrast, responses estimated from the CM5 data exhibit lower
 158 coherencies for periods < 90 days, but due to longer time series (≈ 12 years), longer periods
 159 up to 177 days are better resolved. This motivated our decision to combine responses from
 160 different missions. Additionally, we used magnetic signals due to the semi-diurnal M_2 lunar
 161 tide extracted from 12 years of satellite data [Sabaka *et al.*, 2015]. The radial magnetic field
 162 component (Figure 3) of this signal was used in the inversion.



163 **Figure 2.** C_1 responses and their squared coherences estimated from Swarm (Nov 2013 - Dec 2016) and
 164 CM5 data (CHAMP, Oersted, SAC-C). Positive and negative values represent real and imaginary parts of the
 165 response, respectively.

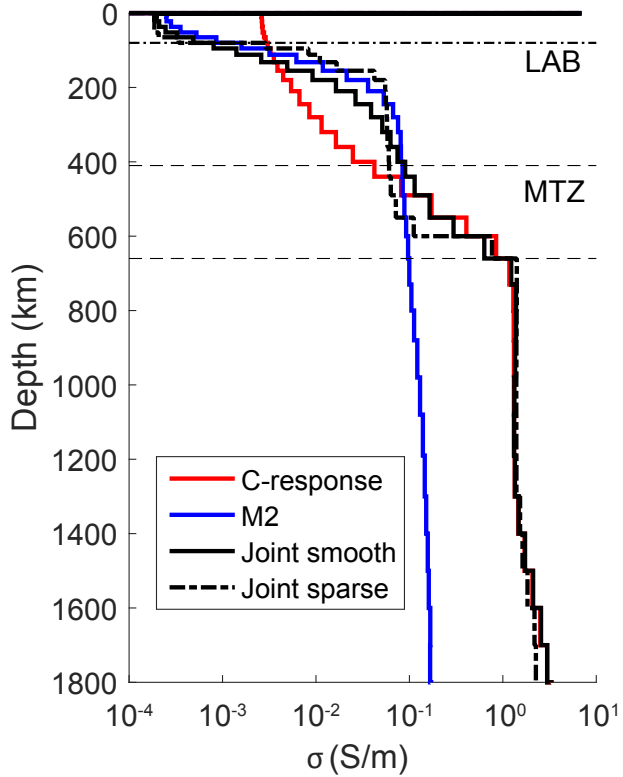


166 **Figure 3.** Real (a) and imaginary (b) parts of the radial magnetic field component due to semi-diurnal M_2
 167 tide at 430 km altitude. Standard deviation of the signals is shown in (c), note different scale.

168 3.2 Inversion

169 In this study, the subsurface was parametrized using 45 layers ranging in thickness
 170 from 9 km right under the oceans and continents to 120 km at the core-mantle boundary
 171 where a metal conductor ($\sigma = 10^5$ S/m) is assumed. The starting model was a homogeneous
 172 spherical shell of 0.2 S/m.

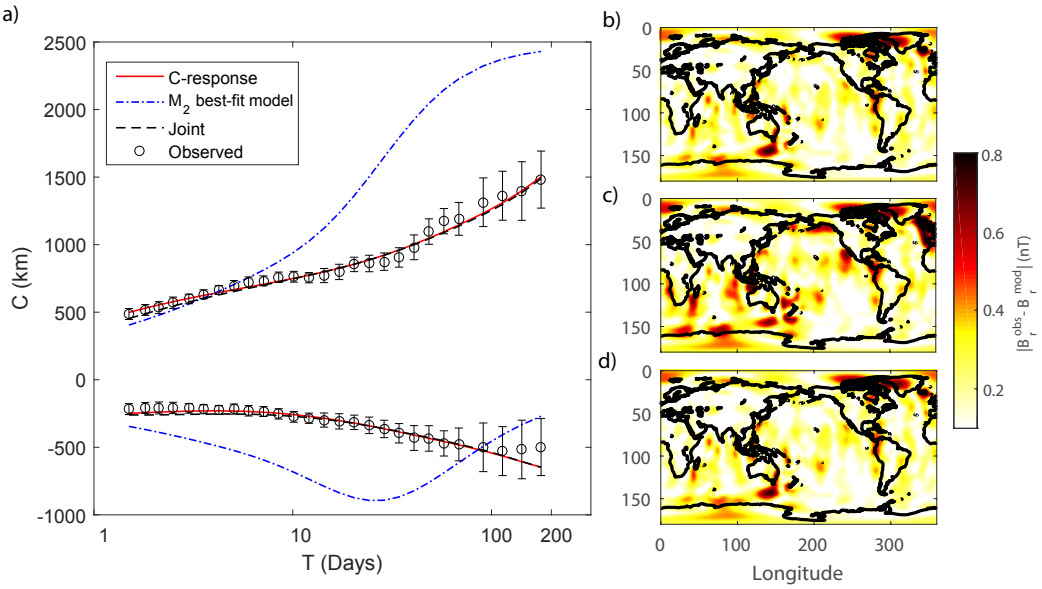
173 Figure 4 shows models obtained by inverting satellite magnetospheric and ocean tidal
 174 signals separately and jointly. Notably, inversion of C_1 -responses fails to recover a prominent
 175 boundary between the lithosphere and astenosphere, which results from the lack of resolution
 176 in the upper mantle [Pütthe *et al.*, 2015b]. This is not surprising given that the shortest period
 177 for C_1 -responses is 1.5 days (Figure 2). In contrast, the conductivity model obtained by in-



173 **Figure 4.** Global conductivity models derived from separate and joint inversions of satellite data. The C -
 174 response profile denotes the model obtained by inverting magnetospheric ring current responses and the M_2
 175 model denotes the global profile derived from the magnetic tidal signals due to semi-diurnal M_2 tide. Joint
 176 inversions were performed using smoothing and structurally sparse (L_1 -norm) regularization. Individual models
 177 were calculated with smoothing regularization. For reference, values for the average lithosphere-asthenosphere
 178 boundary under the oceans and mantle transition zone are plotted as dashed horizontal lines.

184 inverting tidal magnetic signals displays a sharp conductivity increase around the lithosphere-
 185 asthenosphere boundary (LAB) at the depth of 70-80 km, but does not show any large varia-
 186 tions below ≈ 300 km, where it attains a value close to the initial conductivity model. The
 187 models obtained from the joint inversion of magnetospheric C_1 -responses and tidal mag-
 188 netic signals managed to resolve the LAB and at the same time constrain conductivity of the
 189 mantle transition zone (MTZ) and below. We used different types of regularization norms
 190 to produce smooth and structurally sparse models. Both models fit data virtually equally
 191 well, attesting to the non-uniqueness of the inverse problem and data uncertainties.

197 Let us now examine the data responses these models produce. Figure 5(a) shows ob-
 198 served C_1 -responses as well as responses calculated using the models from Figure 4. One
 199 sees that the responses calculated for the models derived from the inversion of C_1 -responses
 200 alone and the joint inversion model fit data within uncertainties, whereas the M_2 model pro-
 201 duces substantially different responses. While the real part of C_1 -responses for the M_2
 202 model is close to the observed data for periods < 10 days, the imaginary part differs for all
 203 periods. This behaviour is confirmed through synthetic tests (see supplementary material)
 204 and is to be expected since the M_2 model is not forced to fit C_1 -responses. Further, Figure
 205 5(b-d) shows absolute residuals between observed and predicted tidal magnetic signals. Here
 206 we see that the residuals are systematically larger for the C_1 -response model (Figure 5c), with



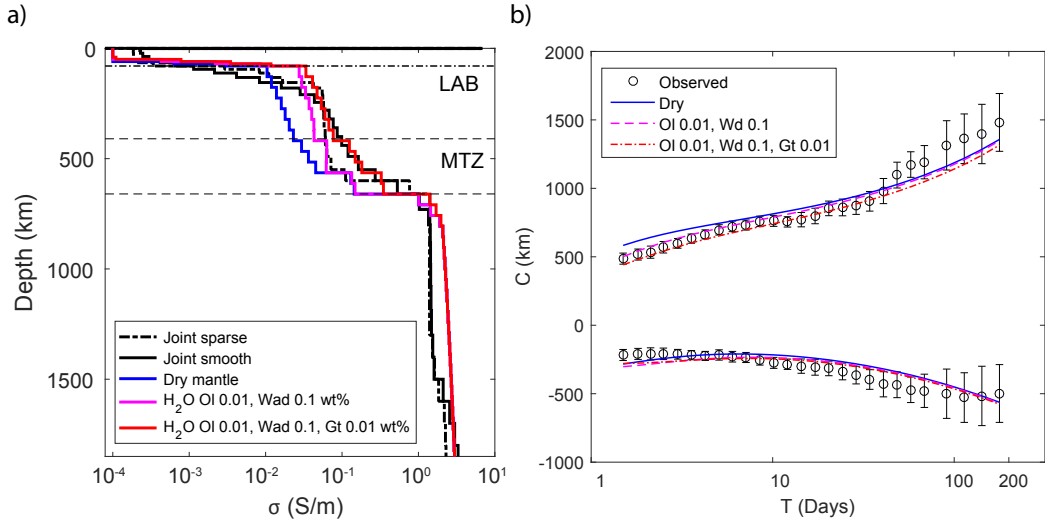
192 **Figure 5.** (a) Observed and calculated global C_1 -responses for models shown in Figure 4. Positive and
 193 negative values represent real and imaginary parts of the response, respectively. (b-d) Magnitude of the radial
 194 magnetic field component residuals between observed tidal signals and their predicted counterparts for the
 195 models shown in Figure 4: models obtained by inverting tidal magnetic signals only (b), magnetospheric
 196 C_1 -responses only (c) and both simultaneously (d).

207 differences reaching up 40% of the original signal amplitude. For instance, the residuals are
 208 large in regions around South Africa, west of Australia, around New Zealand, west of Cal-
 209 ifornia, south of Alaska. This suggests that the increase in conductivity at the LAB that is
 210 missing in this model is required to explain the data. Indeed, and as expected, both the M_2
 211 and joint inversion models explain tidal magnetic signals equally well (cf. Figure 5b and 5d).
 212 Note that since joint smooth and sparse models produce virtually identical responses, only
 213 smooth model responses are shown in Figure 5.

214 3.3 Comparison with laboratory-based conductivity profiles

215 Joint inversion models seem to constrain upper and mid-mantle conductivities bet-
 216 ter than individual inversions. Therefore, it is instructive to interpret these models. To this
 217 end, we compute laboratory-based bulk electrical conductivity profiles using the approach of
 218 *Khan* [2016]. Bulk electrical conductivity is estimated from the mineralogy and databases
 219 of laboratory mineral conductivity measurements. Whereas equilibrium rock mineralogy,
 220 including elastic moduli and density, is computed by free-energy minimization [Connolly,
 221 2009] as a function of pressure, temperature, and bulk composition using the thermo-
 222 dynamic formulation and data compiled by *Stixrude and Lithgow-Bertelloni* [2011]. We model
 223 mantle composition using the $\text{Na}_2\text{O}-\text{CaO}-\text{FeO}-\text{MgO}-\text{Al}_2\text{O}_3-\text{SiO}_2$ chemical system; bulk
 224 rock conductivity and elastic properties are estimated by employing appropriate aver-
 225 aging techniques. The pressure profile is obtained by integrating the load from the surface.
 226 We compute bulk electrical conductivity profiles for a pyrolytic mantle and a standard
 227 temperature of 1390°C at the base of a 80 km thick lithosphere [Katsura *et al.*, 2010]. The
 228 sublithospheric mantle adiabat is defined by the entropy of the lithology at the base of the
 229 lithosphere, whereas in the lithosphere, temperature is computed by a linear geothermal gra-
 230 dient (see supplementary material). Elastic properties and density produced by this thermo-

231 chemical model agree remarkably well with PREM (see supplementary material) of *Dziewon-*
 232 *ski and Anderson [1981].*



233 **Figure 6.** (a) Comparison of conductivity models obtained from inversion of satellite data and several
 234 laboratory-based conductivity profiles calculated following the approach of *Khan [2016]*. The laboratory-
 235 based profiles are based on the assumption of a pyrolytic mantle and different water contents in olivine (OI),
 236 wadsleyite (Wad) and garnet (Gr). (b) Global C_1 -responses calculated for the laboratory-based conductivity
 237 profiles shown in (a). Observed responses are shown with circles. Positive and negative values represent real
 238 and imaginary parts of the response, respectively.

239 Figure 6 shows a number of laboratory-based conductivity profiles calculated for dif-
 240 ferent mantle mineral water contents and plotted together with the joint inversion results. For
 241 present purposes, we varied the water content of olivine, garnet, and wadsleyite. The wa-
 242 ter contents of clinopyroxene, orthopyroxene, and ringwoodite are estimated using the water
 243 partition coefficients described in *Khan [2016]*, which are based on the measurements of *In-*
 244 *oue et al. [2010]* and *Férot and Bolfan-Casanova [2012]*. As is evident from the figure, a
 245 dry mantle produces conductivities which are much lower than the conductivity of the mod-
 246 els obtained from the joint inversion. Moderate amounts of water [*Karato, 2011; Khan and*
 247 *Shankland, 2012*], 0.01 wt% in olivine and 0.1 wt% in wadsleyite, in the upper mantle and
 248 transition zone results in conductivities which are much closer to the inverted models. An
 249 increase of 0.01 wt% in the water content of garnet results in higher conductivities through-
 250 out the upper mantle and MTZ improving the match to the smooth model and observations
 251 (Figure 6b). However, these differences are likely within the uncertainty of our models and
 252 should be considered with caution. The conductivity of the lower mantle in the inverted
 253 models is close to the laboratory predictions.

254 While this interpretation is qualitative and a direct inversion in terms of thermo-chemical
 255 parameters is more appropriate [*Khan, 2016*], these results stress that conductivity models
 256 obtained from joint inversion of data from very different sources produce self-consistent
 257 models. The thermo-chemical modeling combined with laboratory measurements of the
 258 electrical conductivity further confirms that these models are consistent with plausible man-
 259 tle properties and moderate water contents, in addition to radial seismic reference models
 260 (see supplementary material).

261 **4 Conclusions**

262 The inversion of natural source EM data for Earth's mantle electrical conductivity
 263 usually relies on single-source data and therefore faces the problem of limited resolution at
 264 different depths due to limits in frequency range imposed by varying source morphology.
 265 We showed that inverting data from magnetospheric and ocean tidal sources simultaneously
 266 yields a consistent conductivity profile of the upper mantle and transition zone. The obtained
 267 global profile is capable of fitting individual data types as well as separate inversions and
 268 efficiently exploits sensitivity overlap between different sources.

269 The new conductivity profile provides additional constraints on estimations of geo-
 270 physically relevant mantle properties through comparisons with laboratory-based conduc-
 271 tivity profiles. Specifically, assuming a pyrolytic mantle composition and the temperature of
 272 $T = 1380^{\circ}\text{C}$ at LAB we found that a moderate amount of water is necessary to explain the
 273 observed conductivity values in the astenosphere and MTZ. However, for the upper mantle,
 274 this profile is more representative of the mantle under the oceans since tidal signals are neg-
 275 ligible above continents. Taking these points into account, the new model can serve as a new
 276 reference for studies, which need to account for mantle conductivity such as in space weather
 277 or oceanography. Finally, the approach of jointly inverting multi-source data can significantly
 278 help studies that aim at mapping lateral variations in mantle conductivity.

279 **Acknowledgments**

280 We thank ESA for access to the Swarm data. This work was supported by the ESA's Support
 281 to Science Element program. All data responses and models can be obtained upon request to
 282 the authors. This work was supported by a grant from the Swiss National Supercomputing
 283 Centre (CSCS) under project ID660.

284 **References**

285 Bahr, K., N. Olsen, and T. J. Shankland (1993), On the combination of the magnetotelluric
 286 and the geomagnetic depth sounding method for resolving an electrical conductivity in-
 287 crease at 400 km depth, *Geophysical Research Letters*, 20(24), 2937–2940.

288 Civet, F., E. Thébault, O. Verhoeven, B. Langlais, and D. Saturnino (2015), Electrical con-
 289 ductivity of the Earth's mantle from the first Swarm magnetic field measurements, *Geo-
 290 physical Research Letters*, 42(9), 3338–3346.

291 Connolly, J. (2009), The geodynamic equation of state: what and how, *Geochemistry, Geo-
 292 physics, Geosystems*, 10(10).

293 Dziewonski, A. M., and D. L. Anderson (1981), Preliminary reference Earth model, *Physics
 294 of the earth and planetary interiors*, 25(4), 297–356.

295 Egbert, G. D., J. R. Booker, and A. Schultz (1992), Very long period magnetotellurics at
 296 Tucson Observatory: Estimation of impedances, *Journal of Geophysical Research: Solid
 297 Earth*, 97(B11), 15,113–15,128.

298 Everett, M. E., S. Constable, and C. G. Constable (2003), Effects of near-surface conduc-
 299 tance on global satellite induction responses, *Geophysical Journal International*, 153(1),
 300 277–286.

301 Férot, A., and N. Bolfan-Casanova (2012), Water storage capacity in olivine and pyroxene
 302 to 14GPa: Implications for the water content of the Earth's upper mantle and nature of
 303 seismic discontinuities, *Earth and Planetary Science Letters*, 349, 218–230.

304 Grayver, A. V., and A. V. Kuvshinov (2016), Exploring equivalence domain in non-linear
 305 inverse problems using Covariance Matrix Adaption Evolution Strategy (CMAES)
 306 and random sampling, *Geophysical Journal International*, 205, 971–987, doi:
 307 10.1093/gji/ggw063.

308 Grayver, A. V., N. R. Schnepf, A. V. Kuvshinov, T. J. Sabaka, C. Manoj, and N. Olsen
 309 (2016), Satellite tidal magnetic signals constrain oceanic lithosphere-asthenosphere

boundary, *Science Advances*, 2(9), e1600,798.

Inoue, T., T. Wada, R. Sasaki, and H. Yurimoto (2010), Water partitioning in the Earth's mantle, *Physics of the Earth and Planetary Interiors*, 183(1), 245–251.

Karato, S.-i. (2011), Water distribution across the mantle transition zone and its implications for global material circulation, *Earth and Planetary Science Letters*, 301(3), 413–423.

Katsura, T., and T. Yoshino (2015), Heterogeneity of Electrical Conductivity in the Oceanic Upper Mantle, in *The Earth's Heterogeneous Mantle*, pp. 173–204, Springer International Publishing.

Katsura, T., A. Yoneda, D. Yamazaki, T. Yoshino, and E. Ito (2010), Adiabatic temperature profile in the mantle, *Physics of the Earth and Planetary Interiors*, 183(1), 212–218.

Key, K. (2016), MARE2DEM: a 2-D inversion code for controlled-source electromagnetic and magnetotelluric data, *Geophysical Journal International*, 207(1), 571–588.

Khan, A. (2016), On earth's mantle constitution and structure from joint analysis of geo-physical and laboratory-based data: An example, *Surveys in Geophysics*, 37(1), 149–189, doi:10.1007/s10712-015-9353-z.

Khan, A., and T. Shankland (2012), A geophysical perspective on mantle water content and melting: Inverting electromagnetic sounding data using laboratory-based electrical conductivity profiles, *Earth and Planetary Science Letters*, 317, 27–43.

Kuvshinov, A. (2008), 3-D global induction in the oceans and solid earth: recent progress in modeling magnetic and electric fields from sources of magnetospheric, ionospheric and oceanic origin, *Surveys in Geophysics*, 29(2), 139–186.

Kuvshinov, A., and N. Olsen (2006), A global model of mantle conductivity derived from 5 years of CHAMP, Ørsted, and SAC-C magnetic data, *Geophysical Research Letters*, 33(18).

Olsen, N. (1999), Long-period (30 days–1 year) electromagnetic sounding and the electrical conductivity of the lower mantle beneath Europe, *Geophysical Journal International*, 138(1), 179–187.

Olsen, N., E. Friis-Christensen, R. Floberghagen, P. Alken, C. D. Beggan, A. Chulliat, E. Doornbos, J. T. Da Encarnaçāo, B. Hamilton, G. Hulot, et al. (2013), The Swarm satellite constellation application and research facility (SCARF) and Swarm data products, *Earth, Planets and Space*, 65(11), 1189–1200.

Pütthe, C., and A. Kuvshinov (2013), Determination of the 1-D distribution of electrical conductivity in Earth's mantle from Swarm satellite data, *Earth, Planets and Space*, 65(11), 1233–1237.

Pütthe, C., A. Kuvshinov, and N. Olsen (2015a), Handling complex source structures in global EM induction studies: from C-responses to new arrays of transfer functions, *Geophysical Journal International*, 201(1), 318–328.

Pütthe, C., A. Kuvshinov, A. Khan, and N. Olsen (2015b), A new model of earth's radial conductivity structure derived from over 10 yr of satellite and observatory magnetic data, *Geophysical Journal International*, 203(3), 1864–1872.

Sabaka, T. J., N. Olsen, R. H. Tyler, and A. Kuvshinov (2015), CM5, a pre-Swarm comprehensive geomagnetic field model derived from over 12 yr of CHAMP, Ørsted, SAC-C and observatory data, *Geophysical Journal International*, 200(3), 1596–1626.

Sabaka, T. J., R. H. Tyler, and N. Olsen (2016), Extracting ocean-generated tidal magnetic signals from Swarm data through satellite gradiometry, *Geophysical Research Letters*, 43(7), 3237–3245.

Shore, R., K. Whaler, S. Macmillan, C. Beggan, J. Velímský, and N. Olsen (2016), Decadal period external magnetic field variations determined via eigenanalysis, *Journal of Geophysical Research: Space Physics*, 121(6), 5172–5184.

Stixrude, L., and C. Lithgow-Bertelloni (2011), Thermodynamics of mantle minerals-II. Phase equilibria, *Geophysical Journal International*, 184(3), 1180–1213.

Velímský, J., Z. Martinec, and M. E. Everett (2006), Electrical conductivity in the Earth's mantle inferred from CHAMP satellite measurements – I. Data processing and 1-D inversion, *Geophysical Journal International*, 166(2), 529–542.